

# JGR Solid Earth

## RESEARCH ARTICLE

10.1029/2023JB028143

### Key Points:

- A high-resolution 3-D crustal velocity model is constructed in the southern portion of the eastern North American margin
- A transitional crust is observed from ocean to continent that was likely formed by a magmatic-assisted continental rifting
- Three high velocity anomalies are observed within the continental crust, probably representing magmatic intrusion associated with Central Atlantic Magmatic Province

### Supporting Information:

Supporting Information may be found in the online version of this article.

### Correspondence to:

C. Yu,  
yucq@sustech.edu.cn

### Citation:

Li, C., & Yu, C. (2024). Seismic evidence for crustal magmatic intrusion beneath the southern part of the eastern North American margin. *Journal of Geophysical Research: Solid Earth*, 129, e2023JB028143. <https://doi.org/10.1029/2023JB028143>

Received 25 OCT 2023

Accepted 15 MAY 2024

### Author Contributions:

**Conceptualization:** Cong Li, Chunquan Yu

**Data curation:** Cong Li

**Formal analysis:** Cong Li

**Funding acquisition:** Cong Li, Chunquan Yu

**Investigation:** Cong Li

**Methodology:** Cong Li

**Supervision:** Chunquan Yu

**Validation:** Cong Li

**Visualization:** Cong Li

**Writing – original draft:** Cong Li

**Writing – review & editing:** Cong Li, Chunquan Yu

## Seismic Evidence for Crustal Magmatic Intrusion Beneath the Southern Part of the Eastern North American Margin

Cong Li<sup>1</sup>  and Chunquan Yu<sup>1,2</sup> 

<sup>1</sup>Department of Earth and Space Sciences, Southern University of Science and Technology, Shenzhen, China, <sup>2</sup>Guangdong Provincial Key Laboratory of Geophysical High-resolution Imaging Technology, Southern University of Science and Technology, Shenzhen, China

**Abstract** The southern portion of the eastern North American margin (SENAM) is an archetypical volcanic passive margin formed during Mesozoic rifting. How past magmatic events affect the evolution of the SENAM remains an open question of fundamental importance. To better understand this question, here we construct a high-resolution 3-D crustal velocity model from the oceanic side to the continental interior with a combination of multimodal dispersion inversion and full-waveform ambient noise tomography. Our new model reveals an oceanic-continental transitional crust over a short horizontal distance of 100–150 km across the SENAM, with a local-scale lower-than-surrounding velocity anomaly directly beneath the transitional crust. Furthermore, the new model shows three intra-crustal higher-than-average velocity anomalies beneath the SENAM continent. We suggest that the magmatism assisted the Mesozoic rifting process to form the narrow ocean-continent transitional crust along the coastline. The underplating of magma beneath the transitional crust led to a reduction of seismic velocity of the uppermost mantle. In addition, it is probable that the emplacement of the Central Atlantic Magmatic Province caused widespread magmatic intrusions within the continental crust of the SENAM, which were later solidified into intra-crustal high-velocity plutons. Our findings provide new insights into crustal modification history at the passive margin.

**Plain Language Summary** It has been suggested that the emplacement of magma played a key role in the formation and evolution of passive margins. However, how this process evolves during geological time is still unclear. The southern portion of the eastern North American margin (SENAM) preserved many magmatic records, making it an ideal laboratory to study this question. In this study, we constructed a high-resolution 3-D crustal velocity model from the oceanic side to the continental interior of the SENAM using a combination of state-of-the-art multimodal dispersion inversion and full-waveform ambient noise tomography. Our new model reveals two important features within the crust and upper mantle of the SENAM: (a) a sharp increase in crustal thickness over a transitional zone from ocean to continent, and a lower-than-surrounding velocity anomaly beneath the eastern margin of the transitional crust; and (b) three higher-than-average velocity anomalies within the continental crust. We suggest that the magmatic events assisted a continental rifting at ~200 Ma in forming the ocean-continent transitional crust. In addition, the magma associated with the emplacement of Central Atlantic Magmatic Province might have been injected into the continental crust of the SENAM, which subsequently solidified into high-velocity igneous rocks.

## 1. Introduction

The southern portion of eastern North American margin (SENAM) is a typical volcanic passive margin, preserving records of magmatic activities over past millions of years from offshore to onshore (Figure 1; Withjack et al., 2013). In the offshore area, a strong positive magnetic anomaly and a gravity anomaly run roughly parallel to the coastline, likely indicating the rifting-related magmatic intrusion within the crust (Figure 1; e.g., Behn & Lin, 2000; Davis et al., 2018; Talwani et al., 1995; Wyer & Watts, 2006). Several second-order gravity and magnetic anomalies are noted onshore, while their origins are enigmatic (Figures 1b and 1c). In the coastal plain, abundant basaltic dikes and sills are distributed approximately in the N-S and NE-SW direction, which was caused by the syn-rifting emplacement of the Central Atlantic Magmatic Province (CAMP), the Earth's largest igneous province (e.g., Marzoli et al., 1999, 2018; McHone et al., 2005). Additionally, two ancient volcanoes are found near the southern Appalachians, whose formation is thought to be associated with post-rift magmatism (Figure 1a; Mazza et al., 2014, 2017).

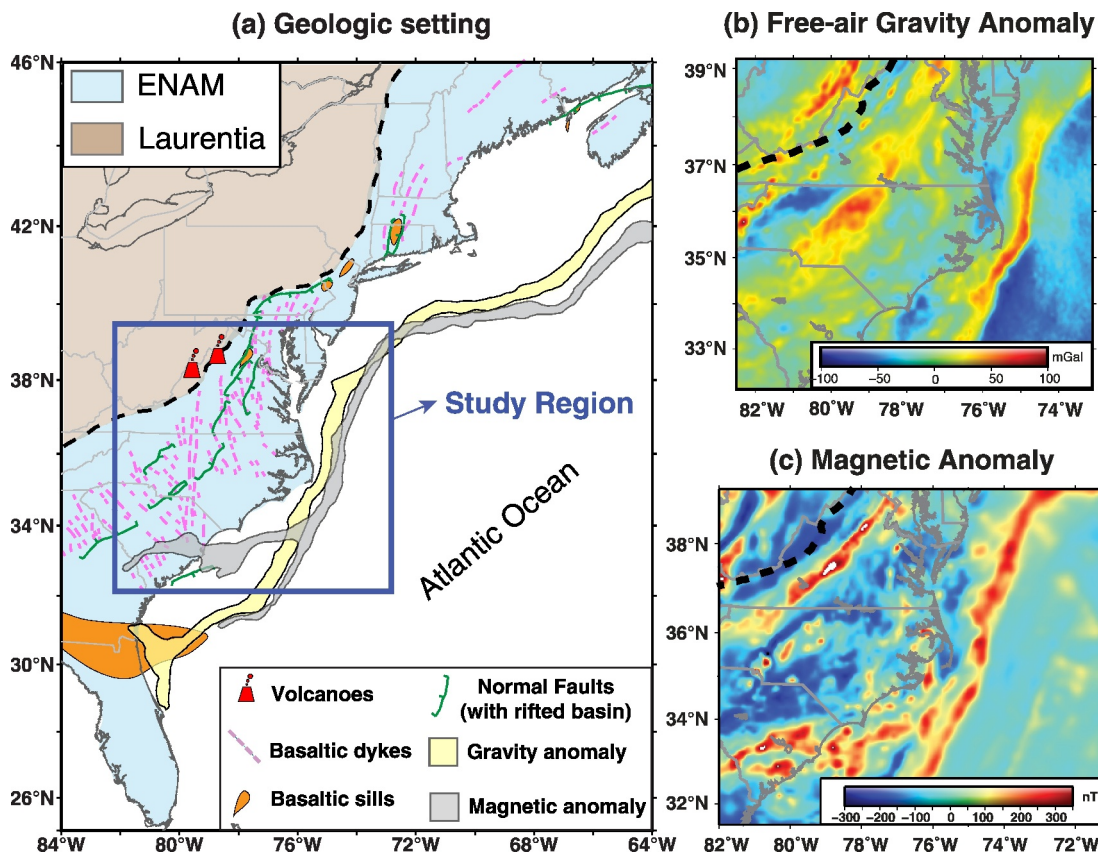


**Figure 1.** (a) Geological map showing the major tectonic units and rift-related features in the eastern North America passive margin (ENAM). The thick black dashed line marks the tectonic boundary between the ENAM and the Laurentia craton and the thin gray solid lines mark the state boundaries. The orange patches represent the basaltic sills, and the pink dashed lines indicate and basaltic dykes, modified from Withjack et al. (2013). The yellow and gray patches represent the offshore gravity and magnetic anomalies showing in (b) and (c), respectively. The green lines represent the normal faults. The red cones represent the post-rifting volcanoes. The blue box indicates our study region. (b) Free-air gravity anomaly map based on Bonvalot et al. (2012) (c) Magnetic anomaly map from Bankey et al. (2002). The black dashed line in (b) and (c) indicates the tectonic boundary that is the same as (a).

Fundamental questions remain regarding the interaction between magmatism and tectonics at the SENAM. For example, some studies suggest that continental rifting led to a significant lithospheric thinning beneath the SENAM, causing magmatic intrusion and the subsequent emplacement of the CAMP (e.g., Daniels et al., 2014; Gao et al., 2020; Marzen et al., 2020). The intruded magmas in turn can facilitate the continental break-up (Bialas et al., 2010; Dick et al., 2003; Pagli et al., 2015; Wright et al., 2012). In contrast, others argue that the CAMP is caused by either plumes or continental temperature insulation and thus is independent of the rifting process (e.g., Coltice et al., 2007; Hole, 2015; Torsvik et al., 2010). Moreover, regional-scale asthenospheric upwelling due to edge-driven convection or lithospheric delamination is also suggested to contribute to the formation of the CAMP (e.g., King & Anderson, 1995; Mazza et al., 2017; McHone, 2000; McHone et al., 2005). Igneous intrusions (i.e., plutons) serve as major inputs into crust from magmatism. Investigating the spatial extent of plutons at depth can thus help understand the total volume of magma involved in past magmatism as well as consider possible causal relationships between rifting, CAMP, and mantle dynamics at the SENAM.

Many seismic tomographic studies have been conducted in the SENAM in order to explore its subsurface structures (e.g., Li et al., 2021; Lynner & Porritt, 2017; Marzen et al., 2020; Russell & Gaherty, 2021). However, the three-dimensional (3-D) fine-scale crustal structures of the SENAM remain poorly constrained, largely limited by data distribution and the resolution of traditional imaging approaches. Several advanced techniques, such as multimodal dispersion inversion (e.g., Hu et al., 2020; Wang et al., 2019; Wu et al., 2020) and full-waveform ambient noise tomography (e.g., Gao & Shen, 2014; Savage et al., 2017), have been developed in recent years to effectively improve the vertical and horizontal imaging resolution of crustal velocity structures. In this study, we combine these two methods to construct a new high-resolution 3-D crustal velocity model of the

SENAM, based on available seismic data from the oceanic side to the continental interior. Our new model allows us to explore the 3-D distribution of magmatic intrusion within the crust of the SENAM and to estimate the volume of intruded magmas, which provides important insights into the evolution at the passive margin.

## 2. Background

### 2.1. Tectonic Settings

The formation and evolution of the SENAM involve multiple tectonic events from the assembly of the Pangea supercontinent to its breakup over the past 500 million years (Figure 1a; Withjack et al., 2013). Between ~270 and ~495 Ma, a sequence of island arcs and microcontinents accreted onto the Laurentia craton, along with the subsequent collision with the Gondwana continent, leading to the assembly of Pangea (Figure 1a; Hatcher, 2010). Extensive continental rifting initiated at ~230 Ma, accompanied by the formation of multiple normal faults and rift basins (Leleu & Hartley, 2010; Withjack et al., 2013). During rifting, the CAMP was emplaced along the margin over a short period of less than 1 million years at ~201 Ma (Marzoli et al., 1999, 2018). The western limit of the CAMP in the SENAM runs roughly along the southern Appalachian Front interpreted as the boundary between the Laurentia craton and the passive margin, and its eastern limit could extend as far as the continental shelf (Figure 1a; Marzoli et al., 2018). The rift-to-drift transition initiated ~3–5 million years before the CAMP and was completed by ~170 Ma, with an initial spreading center currently situated as far as ~200 km offshore (Shuck et al., 2019; Withjack et al., 2013). Afterward, several periods of localized post-rifting volcanism occurred in the SENAM between ~152 and ~47 Ma, and the current passive margin was eventually established (e.g., Bailey & Lupulescu, 2015; Kinney et al., 2021; Mazza et al., 2017).

### 2.2. Previous Studies

Many previous studies have revealed the first-order crustal structures beneath the SENAM. For example, offshore active-source seismic surveys image strong seaward dipping reflectors in the crystalline basement of the continental shelf that are interpreted as volcanic rocks extruded during the continental spreading (e.g., Austin et al., 1990; Lang et al., 2020; Sheridan et al., 1993). Beneath the reflectors, high velocity lower crust is observed in the seismic refraction profiles, probably representing a local mafic intrusion and/or underplating beneath the crust (e.g., Becel et al., 2020; Holbrook et al., 1994). The current Moho depth increases from ~17 to 20 km in the oceanic side into ~25–30 km in the coastal plain and ~40–50 km in the southern Appalachians (e.g., Becel et al., 2020; Li et al., 2020; Lynner & Porritt, 2017; Ma & Lowry, 2017; Shuck et al., 2019). Beneath the inland continental crust, a local-scale high velocity lower crustal layer has been detected in the southern Georgia rift basins, which is probably associated with the magmatic underplating during the CAMP emplacement (Marzen et al., 2020). Nevertheless, previous studies are limited either by spatial coverage or by model resolution. As a result, there remains a lack of comprehensive, high-resolution investigations of the crustal structures beneath the SENAM.

## 3. Data and Methodology

We collected continuous vertical-component seismic waveforms recorded between January 2000 and May 2022 from a total of 245 broadband land stations and 30 broadband oceanic bottom stations (OBSs, Figure 2a). These stations are from 10 long-running networks and 6 temporary dense arrays. In this study, we first retrieved the empirical Green's functions (EGFs) between each station pair from the ambient noise data (Section 3.1). We then constructed a 3-D S-wave velocity model through a two-step procedure: (a) We obtain an initial velocity model by inverting the multimodal dispersion curves of Rayleigh waves extracted from ambient noise (Sections 3.2 and 3.3); (b) We iteratively refine the velocity model with full-waveform ambient noise tomography until the model is stable (Section 3.4).

### 3.1. Retrieval of Empirical Green's Functions

We retrieved the EGFs by cross-correlating the ambient noise recorded by each station pair. Before cross-correlation, we observed strong compliance and tilt noises in the OBS data that were associated with the vertical and horizontal pressures of the ocean currents (Figures S1 and S2 in Supporting Information S1). These water-related noises can significantly impact the recovery of the EGFs (e.g., Bowden et al., 2016; Russell & Gaherty, 2021). We thus first removed both types of noise from the vertical components at OBSs (Figures S2 and S3

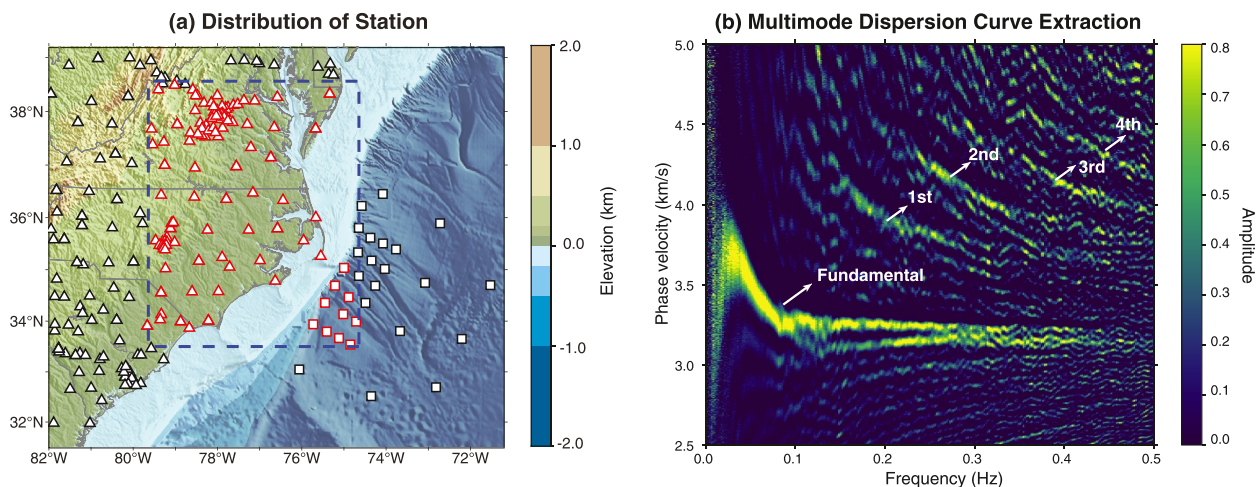


**Figure 2.** (a) Distribution of the broadband seismic stations used in this study. Triangles represent the land stations, and the squares represent the Ocean Bottom Seismic stations (OBSs). The stations for calculating the frequency-phase velocity spectrum of empirical Green's Functions (EGFs) in (b) are highlighted with red colors in the blue dashed box. The background color is the bathymetry/topography. (b) An example of frequency-phase velocity spectrum of EGFs. The high amplitudes marked by arrows indicate the singular points that represent the multimodal dispersion curves.

in Supporting Information S1; Please see the details for the removal of the tilt and compliance noise in Supporting Information S1). We then removed the instrument response at each station, cut data into daily length segments, and normalized the daily records. The EGFs were obtained as the negative time derivatives of the stacked daily cross-correlations.

We observe clear Rayleigh wave signals in the EGFs at periods of 4–100 s for land-ocean and land-land station pairs, and periods of 4–50 s for ocean-ocean station pairs (Figures S3 and S4 in Supporting Information S1). We calculated the signal-to-noise ratio (SNR) for both positive and negative time segments to quantify the quality of EGFs. The SNR is defined as the ratio of the maximum amplitude in each segment of EGFs within the arrival time window of Rayleigh waves to the standard deviation of monthly stacks of cross-correlations. In general, most EGFs exhibit good quality, with a SNR larger than 2. The SNR for some ocean-land and ocean-ocean station pairs show significant variations between positive and negative segments at periods of 4–20 s, which are likely due to the inhomogeneous distribution of shallow-depth noise sources in the ocean (Figures S5 and S6 in Supporting Information S1). Nevertheless, it has been suggested that such asymmetry in the EGFs has a minor effect on the travel time of Rayleigh waves compared to the velocity perturbations of the Earth structures (e.g., Gao & Shen, 2014; Yang & Ritzwoller, 2008). We thus consider our obtained EGFs a close approximation to the real Green's functions of the Earth.

### 3.2. Extraction of Multimodal Dispersion Curves

We obtained the multimodal dispersion curves of Rayleigh waves within our study area using an array-based approach developed by Wang et al. (2019). This technique suggests that, if Rayleigh waves propagate in a homogeneous flat-layered medium, their dispersion curves can be inferred from singular points in their frequency-phase velocity spectrum. And a high-quality frequency-phase velocity spectrum can be calculated by the Fourier-Bessel transform of an ensemble of EGFs.

We divided our study area into multiple overlapping subregions and then calculated the frequency-phase velocity spectrum of a collection of EGFs within each subregion (Figure 2 and Figure S7 in Supporting Information S1). The size of subregion is  $5^\circ \times 5^\circ$  in the longitudinal and latitudinal directions with an overlapping area of  $4^\circ$ . We extracted the multimodal dispersion curves of Rayleigh waves for each subregion by tracing the maximum amplitudes in the frequency-phase velocity spectrum (Figure 2b). We also picked the points with amplitudes equal to 90% of maxima in spectrum as the uncertainty of the dispersion curves. The multimodal dispersion curves can provide more information on the variations of crustal structures in vertical direction compared to the fundamental mode, even though the constraints on horizontal variations are limited due to the averaging effects of the EGF ensemble in each subregion.

Here we provide an example of the extracted multimodal dispersion curves from one of the subregions in our study area (Figure 2). This subregion contains 4,187 EGFs from 131 land and 9 oceanic virtual sources, and their Fourier-Bessel transform shows five distinct traces of singular points that corresponds to the fundamental and 1–4th mode dispersion curves (Figure 2). Specifically, the fundamental mode dispersion curve has a dominant frequency range of  $\sim 0.01$ – $0.18$  Hz. It becomes complex at frequencies greater than 0.18 Hz, likely due to the horizontal variations in shallow-depth structures. We avoid picking these complex singular points in high frequencies so that we can obtain the first-order structures in this region. The 1–4th mode dispersion curves have dominant frequencies of  $\sim 0.18$ – $0.29$ ,  $\sim 0.25$ – $0.4$ ,  $\sim 0.3$ – $0.5$ , and  $\sim 0.36$ – $0.5$  Hz, respectively. Higher modes are hard to identify in the spectrum although they may exist. In most land subregions, we can extract high-quality multimodal dispersion curves of Rayleigh waves (Figure S7 in Supporting Information S1). For the subregions in the oceanic portion, however, we can only extract the fundamental mode, likely due to the large noise in the OBS data and fewer EGFs involved in the calculation of the frequency-phase velocity spectrum.

### 3.3. Inversion for the Initial Velocity Model

The extracted multimodal dispersion curves within each subregion were inverted for a 1-D depth-dependent S-wave velocity profile, and all the profiles were combined to form an initial model. We parametrized the 1-D velocity profile with a sequence of velocity-depth pairs from the surface into a depth of 50 km. In addition to the velocity and the depth, we also searched for the number of layers and the noise level of dispersion curves during inversion. The search ranges for the S-wave velocity, the depth, and the number of layers were set to 1–5 km/s, 0–50 km, and 1–30, respectively, while the range of noise level in the observed dispersion curves was set between 0 and its maximum uncertainty. The  $V_p/V_s$  ratio cannot be well resolved by dispersion curve inversion, so we set it to be a constant value of 1.78 (Ma & Lowry, 2017).

We inverted the 1-D S-wave velocity profile for each subregion using Bayesian-Markov chain-Monte Carlo inversion (e.g., Bodin & Sambridge, 2009; Bodin et al., 2012; Dreiling & Tilmann, 2019). We performed the inversion with 50 Markov chains for a total of 250,000 iterations of inversion. Most chains effectively converge to the global optimum models with misfits close to the minimum value, while a few chains return with large misfits (Figure S8 in Supporting Information S1). We first excluded the chains of local optimum models if their misfits are 5% larger than the minimum value. We then randomly selected 50,000 models in the chains of global optimum and took their average as the 1-D velocity profile for each region (Figure 3). We eventually obtained a total of 106 1-D velocity profiles, and we interpolated these profiles into a pseudo-3-D initial velocity model with a vertical interval of 1 km and a horizontal interval of  $0.5^\circ$ .

### 3.4. Full-Waveform Ambient Noise Tomography

The initial model obtained in Section 3.3 provides first-order constraints on the velocity structures beneath our study area. However, the model has limited resolution for fine-scale variations within the crust due to the assumption of a 1-D layered medium during its construction (Figure 3b). We thus refined the initial model by carrying out full-waveform ambient noise tomography (e.g., Gao & Shen, 2014; Li et al., 2021). Specifically, we first simulated 3-D wave propagation based on the initial model using a nonstaggered-grid, finite difference method, and extracted synthetic Rayleigh waveforms between each station pair. The initial model was parameterized into  $0.015^\circ \times 0.015^\circ$  in the longitudinal and latitudinal directions, and the vertical grid size linearly increases from 0.55 to 3 km downward. We set the sea level as 0 km and the maximum depth at 50 km. In our model configuration, we considered topography and the presence of water in term of bathymetry data, which improves the accuracy of the wavefield simulation.

We then measured the phase delays between the interstation EGFs and the synthetics by calculating their cross-correlation over eight overlapping period bands, ranging within 35–70, 30–60, 25–50, 15–30, 10–20, 7–15, 5–10, and 4–8 s. During the measurement, we required the average SNR between the positive and negative segments of observed EGFs to be  $\geq 6$  for the land-land, and land-ocean station pairs and  $\geq 2$  for the ocean-ocean station pairs. The minimum limit of the correlation coefficients was set to be 0.7 for the land-land and land-ocean station pairs, and 0.65 for the ocean-ocean station pairs. For most station pairs, we separately calculated the phase delays for the positive and negative segments of the EGFs, and took their average as the final measurement result. However, if the SNR in one segment is more than two times larger than the other segment, we will only use the measurement for the segment with a higher SNR ratio.

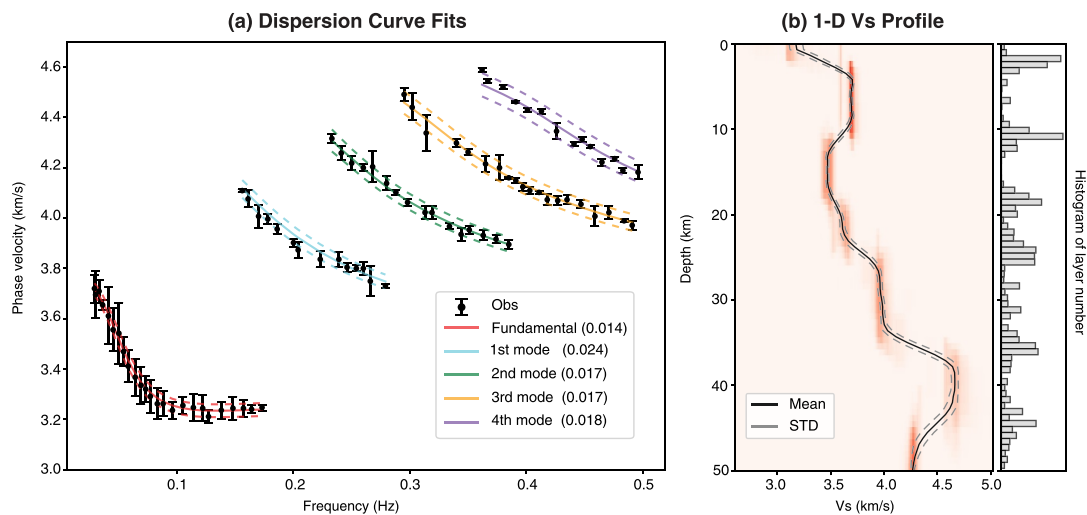


**Figure 3.** (a) Comparison between the observed and synthetic multimodal dispersion curves of Rayleigh waves. The black dots represent observed dispersion curves extracted from Figure 2b, and the error bars indicate their uncertainty. We took the points with a 90% of maximum amplitudes in frequency-phase velocity spectrum as the uncertainty of the extracted dispersion curves. The colored solid lines represent the synthetic multimodal dispersion curves based on the 1-D average velocity profile in (b), whose uncertainties are indicated by the dashed lines. The numbers within parentheses in the legend are the misfits between observations and synthetics for different modes of Rayleigh waves. (b) The inverted 1-D shear velocity profile (left) and the histogram of inverted layer numbers (right). The background color in the left figure indicates the probability density of the velocity and its corresponding depth for a total of 50,000 inverted models. The black solid line represents the average model, and the gray dashed lines represent the standard deviation.

We calculated the 3-D finite-frequency sensitivity kernels of Rayleigh waves for each station pair at the period bands above and inverted for S-wave velocity perturbations using a conjugate gradient method. The final model was obtained by progressively updating the initial model with the calculated velocity perturbations for a total of 5 iterations. Compared to the initial model, our final model shows a significant improvement in both vertical and horizontal resolutions (Figures S10 and S11 in Supporting Information S1). The synthetic waveforms generated by the final model can better predict the Rayleigh waves, with a concentration of delay times approaching near-zero values (Figure 4). The resolution tests show that our model can well resolve the structures with horizontal scale of 50–75 km within the depth range of 4–50 km for the continental portion and the range of 6–40 km for the

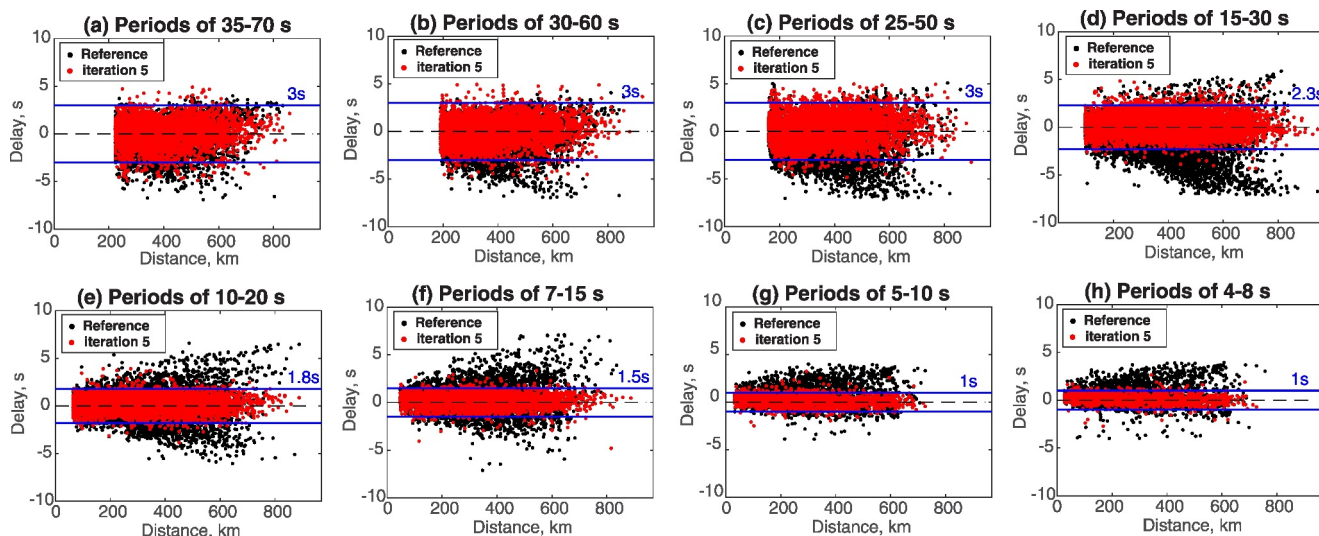


**Figure 4.** Comparison of phase delay time between observed interstation empirical Green's functions and the synthetic waveforms based on the initial model (black dots) and based on the final model (red dots) at multiple periods.

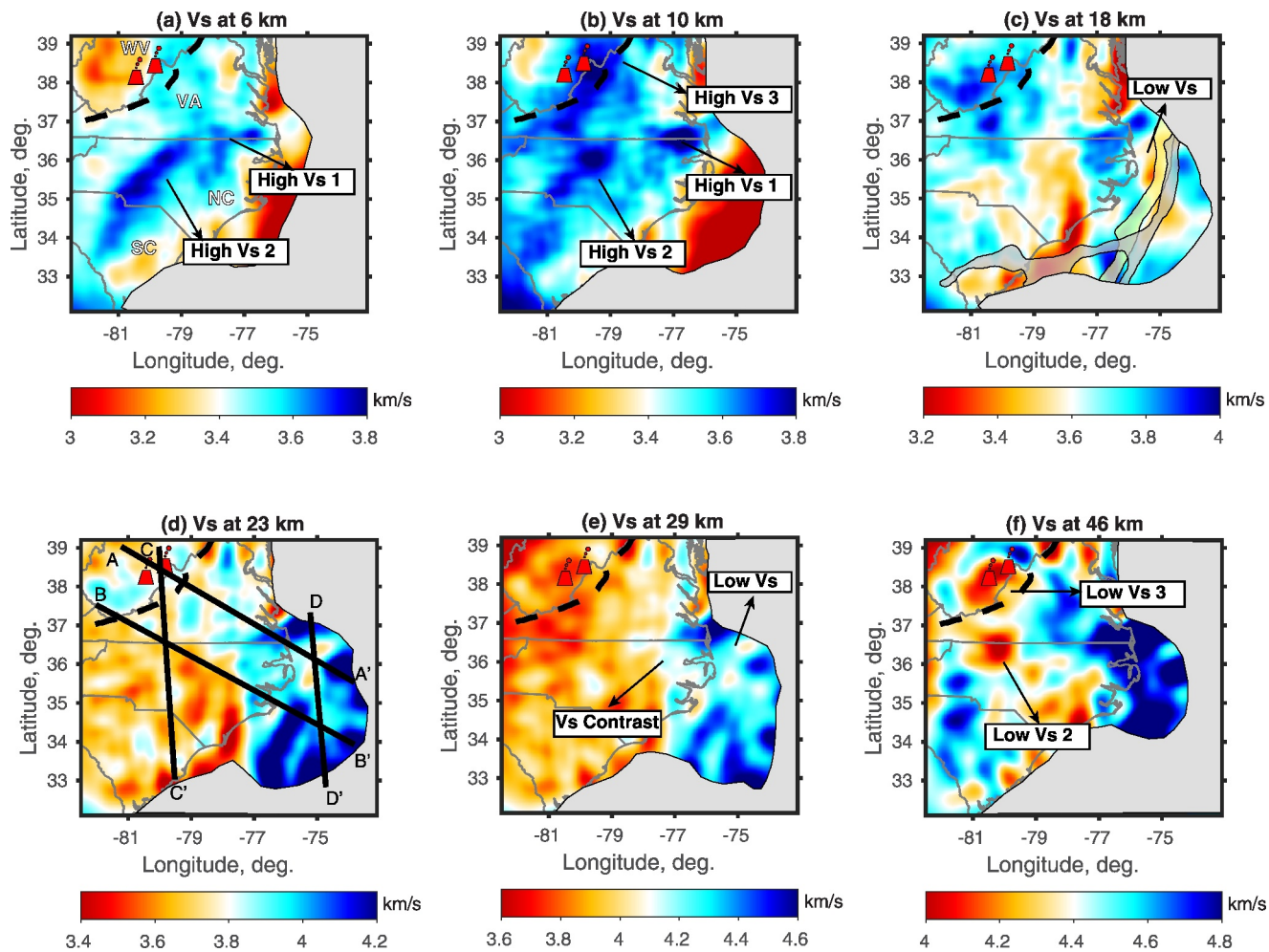


**Figure 5.** Distribution of shear-wave velocity at multiple depths beneath the southern portion of the eastern North American margin. The velocity anomalies are highlighted with texts and arrows. The solid black lines in (d) mark the locations of cross-sections in Figure 6. The abbreviations in (a) indicate the names of states in the U.S. Other symbols are the same as Figure 1.

oceanic portion (Figures S12–S14 in Supporting Information S1; Please see the details of our resolution tests in Supporting Information S1). For velocity perturbations outside of the depth range above, the amplitude of recovered model is underestimated. However, we do not see significant artifacts in the geometry of recovered model.

#### 4. Results

Our new tomographic model images significantly different crustal structures between the oceanic and the continental portion beneath the SENAM. In the oceanic crust, we see a very low S-wave velocity ( $V_s \leq 3.2$  km/s) from the sea floor to the depth of  $\sim 12$  km, which probably represents a thick sedimentary layer (Figures 5a and 5b; Cross-section AA' and BB' in Figure 6). Below the sedimentary layer, S-wave velocity increases sharply from 3.5 km/s at a depth of  $\sim 12$ – $15$ – $4.2$  km/s at a depth of  $\sim 20$ – $25$  km (Cross-section AA' and BB' in Figure 6). The depth range over this vertical velocity gradient is generally consistent with the oceanic Moho depth of  $\sim 17$ – $20$  km observed by previous active-source surveys (e.g., Becel et al., 2020; Lang et al., 2020). In comparison, the continental crust has a low velocity layer ( $V_s \leq 3.2$  km/s) at top  $\sim 5$ – $6$  km depths that concentrates beneath central West Virginia and southeastern South Carolina (Figures 5a and 5b, Cross-section AA' and CC' in Figure 6). The velocity of the continental crust between 6 km depth and 40 km depth is highly heterogeneous, with values varying within a range of 3.2– $4.2$  km/s (Cross-section AA', BB', and CC' in Figure 6). Previous teleseismic receiver function studies (e.g., Li et al., 2020; Ma & Lowry, 2017) and active-source surveys (e.g., Becel

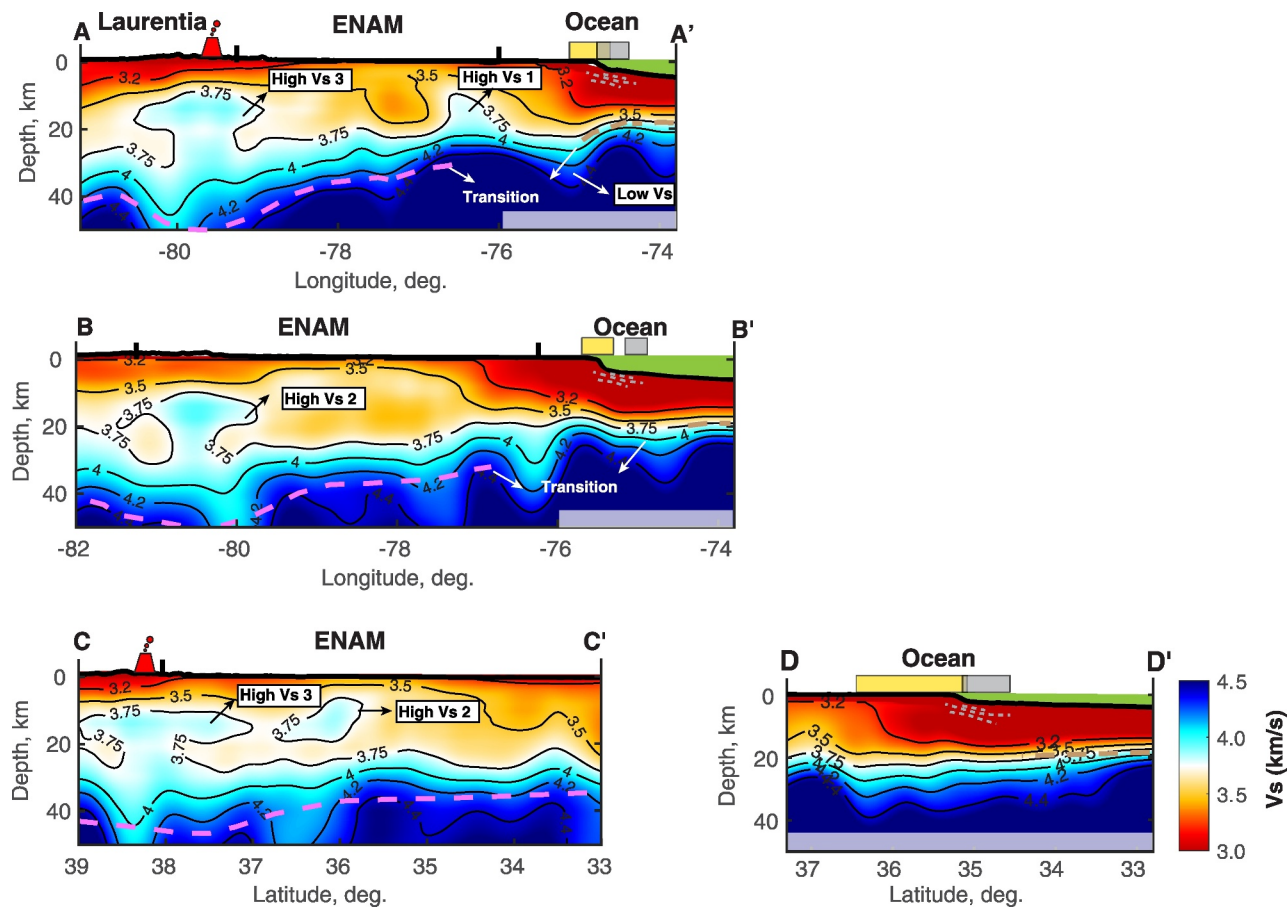


**Figure 6.** Cross-sections of shear-wave velocity beneath the southern portion of the eastern North American margin. The locations of velocity cross-sections are marked in Figure 5d. We set the depth of sea level as 0 km. The pink dashed lines represent the continental Moho depth defined from the tele-seismic receiver function analysis by Li et al. (2020), and the brown dashed lines represent the oceanic Moho depth defined from seismic active-source survey by Becel et al. (2020). The gray dashed lines represent the strong seaward dipping reflectors observed by the active-source seismic survey by Becel et al. (2020). The yellow and gray columns represent the gravity and magnetic anomalies along the coastline, respectively. The green patches represent the water layer. The oceanic portion within the depth range of 45–60 km is masked with white translucent column, due to its relatively poor tomographic resolution. Other symbols are same as Figures 1 and 5.

et al., 2020) show that the Moho depth of the continental crust is ~25–30 km in the coastal plain and continental shelf and ~40–50 km in the southern Appalachians. We observe that the continental Moho depth defined by those studies above roughly follows the 4.2 km/s depth contour in our tomographic model (Cross-section AA', BB', and CC' in Figure 6).

Our model demonstrates a strong lateral variation of S-wave velocity from ocean to continent over a horizontal distance of ~100–150 km across the margin (Figures 5c–5f; Cross-section AA' and BB' in Figure 6). Within a depth range of 0–12 km, the S-wave velocity increases from <3.2 km/s in the oceanic portion to ~3.4–3.8 km/s in the continental portion, which reflects a variation of sedimentary thickness across the margin (Figures 5a and 5b; Cross-section AA' and BB' in Figure 6). At the depths greater than 20 km, we observe a sharp decreasing of velocity from the oceanic portion ( $V_s > 4.0$ ) into the continental portion ( $V_s < 4.0$ ) (Figures 5d and 5e). And this fast-to-slow velocity variation likely represents a transition from the oceanic uppermost mantle to the continental crust, suggesting a significant increase of crustal thickness from ocean to continent (Cross-section AA' and BB' in Figure 6). Additionally, we see a narrow low velocity band (Low  $V_s$ ) immediately below the ocean-continent transitional crust, with a value of ~3.55 km/s at a depth of 18 and ~4.2 km/s at a depth of 30 km, ~5%–6% lower than the surroundings (Figures 5c–5e; Cross-section AA' and BB' in Figure 6).

Our model shows three local-scale high velocity anomalies in the continental crust with values of ~3.7–4.0 km/s, ~6%–10% higher than the surrounding velocity of ~3.5–3.6 km/s (Figure 5; Cross-section AA', BB', and CC' in Figure 6). These anomalies exhibit different horizontal and vertical distributions. The first high velocity anomaly

(High Vs 1) is located in northeastern North Carolina. It has a near-column geometry that spans horizontally  $\sim 100$  km in longitude and  $\sim 100$  km in latitude within the depth range of  $\sim 6$ – $25$  km (Figures 5a–5c; Cross-section AA' in Figure 6). The second anomaly (High Vs 2) is in central North Carolina and South Carolina, whose geometry appears to be a mushroom shape: At a shallow depth of 4–10 km, it distributes along a narrow band in the NE-SW direction, with a horizontal dimension of  $\sim 450 \times 100$  km; At greater depths, its horizontal scale gradually decreases to  $\sim 100 \times 100$  km (Figure 5 and Cross-section BB' in Figure 6). The third anomaly (High Vs 3) is distributed near the state boundary between West Virginia and Virginia. It also has a mushroom-shaped geometry with a tabular head of  $\sim 400 \times 200$  km at a depth of 10–20 km and a tapering root of  $\sim 150 \times 150$  km at greater depths (Figure 5 and Cross-section AA' and CC' in Figure 6). Additionally, we observe localized depression of the Moho beneath High Vs 2 and 3 with depth increasing from  $\sim 40$  km into 50 km (Figure 5f; Cross-section AA', BB', and CC' in Figure 6).

## 5. Discussion

### 5.1. Model Uncertainty and Imaging Resolution

The uncertainties of our model originate from two primary sources. The first source concerns the accuracy of the initial model constructed in Sections 3.2 and 3.3. This uncertainty includes the systematic error involved in picking and inverting the multi-modal dispersion curves, as well as the assumption of a 1-D layered model during inversion. To estimate the systematic error for dispersion curves inversion, we calculate the standard deviation of velocity posterior distribution at each depth for every 1-D profile in the initial model. Our analysis shows that the systematic error in the initial model is less than 2% for most of the continental crust and less than 4% for the oceanic crust (Figure S9 in Supporting Information S1). Furthermore, the uncertainty in the initial model leads to a misfit between synthetic waveforms and the observed EGFs, as evidenced by the relatively disperse distributions of the delay times at different periods (Figure 4). Nevertheless, the subsequent 3-D wavefield simulation and inversion can significantly mitigate the uncertainty of the initial model.

The second uncertainty arises from the non-unique nature of full-waveform tomography. Systematically qualifying this uncertainty poses challenges due to the substantial computational and storage expense. However, the phase delay measurements based on our final model can provide indirect information on its uncertainty. The phase delays based on our final model reveal relatively small values varying within  $\pm 1$  s at periods of 4–10 s, within  $\pm 2$  s at periods of 7–30 s, and within  $\pm 3$  s at long periods of 25–70 s (Figure 4). Our numerical test shows that such delays can correspond to less than 3% of velocity perturbations (Figure S19 in Supporting Information S1), which is much smaller than our key observations described in Section 4.

In addition, we conducted a series of numerical tests to examine the imaging resolution of our model. We first focus on the large phase delays in the initial model that have been significantly corrected by the full-waveform tomography. The seismic ray paths corresponding to those phase delays highlight the region where the resolution can be mostly improved (Figure S15 in Supporting Information S1). The forward modeling tests suggest that correction of those large phase delays can lead to 7%–10% velocity perturbation, consistent with the observed velocity anomalies in our model (Figures S16–S18 in Supporting Information S1). We then conducted two model recovery tests with input velocity anomalies that have the similar scale and geometry to our key observations. Our model recovery test validates that the velocity perturbations with similar dimension and geometry to our key observations can be well recovered (Figures S20 and S21 in Supporting Information S1). In summary, while it is not straightforward to systematically quantify the uncertainties in our model, our analysis demonstrates that the key observations in our model are reliable.

### 5.2. Comparison With Previous Studies

Our new tomographic model shows well-constrained velocity structures of the crust and uppermost mantle beneath the SENAM, with better lateral and vertical imaging resolution compared to previous studies. For example, our model provides a tighter constraint on the sedimentary thickness variation in the SENAM compared to previous tomographic studies (Figures S22 and S23 in Supporting Information S1; e.g., Li & Gao, 2021; Lynner & Porritt, 2017; Shen & Ritzwoller, 2016). The fast-to-slow velocity transition from ocean to continent at the depth of 20–40 km revealed in our model is generally consistent with the observations from previous tomographic studies (e.g., Li & Gao, 2021; Lynner & Porritt, 2017) and matches with the Moho depth variations defined by receiver function studies and active-source surveys (Guo et al., 2019; Holbrook et al., 1994; Li

et al., 2020; Ma & Lowry, 2017). However, our model shows more detailed velocity variations of the crust and the uppermost mantle within this transitional zone (Figures S22 and S23 in Supporting Information S1). Additionally, our model reveals three significantly high-velocity anomalies within the continental crust that have not been recognized by previous studies (Figures S22 and S23 in Supporting Information S1; e.g., Li & Gao, 2021; Shen & Ritzwoller, 2016).

### 5.3. Formation Mechanism for the Oceanic-Continental Transitional Crust

Several key aspects of the oceanic-continental transitional crust observed in our new model suggest an important role of magmatism in its formation and evolution. First, the thickness of both the sedimentary layer and the crust within the transitional zone varies over a horizontal distance of approximately 100–150 km, which is much shorter compared to those in magma-poor passive margins (e.g., Dunbar & Sawyer, 1989; Franke, 2013; Lang et al., 2020). Second, the spatial location of the transitional crust roughly matches with the shallow-depth seaward dipping reflectors representing cool magmatic rocks that are observed by previous active-source seismic surveys (e.g., Austin et al., 1990; Becel et al., 2020; Lang et al., 2020; Sheridan et al., 1993). Third, the presence of Low Vs beneath the eastern boundary of transitional crust spatially aligns with the offshore gravity and magnetic anomalies that are interpreted to be caused by a local-scale magmatic underplating beneath the crust (Figures 5 and 6, e.g., Becel et al., 2020; Holbrook et al., 1994; Lizarralde & Holbrook, 1997).

It has been suggested that the intrusion of high-temperature magma could assist the continental rifting process by reducing the strength of continent lithosphere and promoting the localization of the stretching forces (e.g., Buck, 2004, 2006; Tian & Buck, 2019). Consequently, the magma-assisted stretching forces lead to significant crustal thinning from continent to ocean (Li & Gao, 2021; Lynner & Porritt, 2017). Several recent studies suggest that the magma-assisted rifting in the SENAM experienced a protracted geological time of  $\sim$ 25 million years, leading to a rough basement with scattered magmatic intrusions across the margin (Bécel et al., 2020; Shuck et al., 2019). Our observations are consistent with these previous studies. Furthermore, the underplating of magma can slightly reduce the velocity of uppermost mantle by refertilizing its composition (e.g., Connolly, 2009; Dalton & Faul, 2010; Tian & Buck, 2019; Xu et al., 2008), which well explains the observed local-scale Low Vs beneath the oceanic-continental transitional crust.

### 5.4. High-Velocity Anomalies Within the Continental Crust

#### 5.4.1. Compositional Nature of High-Velocity Anomalies

One of the most striking observations in our study is the intra-crustal anomalies within the SENAM continent, which exhibit a velocity of 3.7–4.0 km/s and display a mushroom/dome-shaped geometry. It has been demonstrated that the emplacement of mafic plutons can significantly increase crustal velocities. For example, laboratory measurements indicate that the Vs velocity of typical plutonic rocks is  $\sim$ 3.7–3.8 km/s (Figure 7; e.g., Christensen & Stanley, 2003). The presence of mantle-derived minerals, such as olivine, spinel and clinopyroxene, can further increase the seismic velocities of plutons into near 4.0 km/s (Kelemen & Holbrook, 1995; Ragland et al., 1992). In addition, laboratory experiments and numerical modeling suggest that both plume- and dome-shaped plutons can be formed during their emplacement, and these geometries can be considered as their characteristic features (e.g., Cao et al., 2016; Cruden & Weinberg, 2018).

We observe a rough spatial correlation between positive gravity data and the near-surface high-velocity anomalies (Figure 8). Specifically, both the Bouguer and Isostatic gravity data reveal a higher-than-surroundings positive anomaly primarily distributed in NE-SW direction along the coastal plain (Figures 8a and 8b). Correspondingly, the portions of High Vs 1 and High Vs 2 at depths shallower than 10 km exhibit a similar horizontal distribution (Figure 8c). The spatial correlation between gravity data and velocity anomalies at greater depths become less prominent, probably due to limited sensitivity of gravity data to deep structures. Nevertheless, an integrative analysis of gravity data and velocity model can provide constraints on the composition of the shallow-depth portion of the observed anomalies, aiding in understanding the nature of entire body. Previous modeling study by Zhang et al. (2020) suggests that a density of  $\sim$ 2.82–2.85 g/cm<sup>3</sup> is required to explain the positive gravity in the coastal plain (Figure S24 in Supporting Information S1). Comparison with typical crustal rocks indicate that density values of high-velocity anomalies fall within a range of intrusive mafic igneous rocks, thus further supporting our hypothesis regarding their compositional nature.

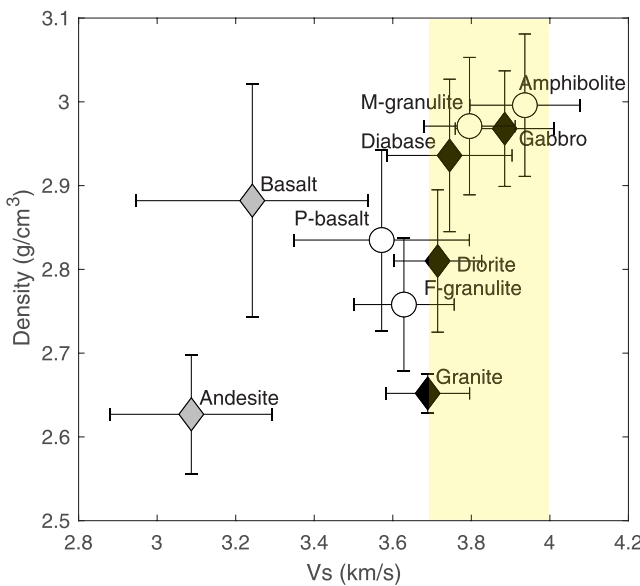


**Figure 7.** Relationship of the Vs values and the density for the typical crustal rocks. The gray and black diamonds mark the Vs and density of typical extrusive and intrusive igneous rocks, respectively. The white circle marks the properties of typical metamorphic rocks within the crust. The properties of crustal rocks above are from the laboratory measurements by Christensen and Stanley (2003). The shaded area marks the value range of the observed high-velocity anomaly in our model.

It has been suggested that asthenospheric upwelling due to local-scale post-rifting delamination/foundering events could emplace magma into the crust and form West Virginia volcanoes (Mazza et al., 2014, 2017). And the solidification of the magma during this process can also account for the observed high-velocity intra-crustal igneous rocks. However, previous imaging studies suggest that the horizontal scale of the magmatic emplacement

due to delamination/foundering events is  $\sim 100 \times 100$  km (e.g., Li et al., 2020; Wagner et al., 2018), much smaller than our observations. It is likely that the CAMP magmatism dominated the formation of plutons in the continental crust of the SENAM. Afterward, one or more asthenospheric upwelling due to local-scale delamination/foundering events further added magma into the crust beneath West Virginia, ultimately leading to current high-velocity anomalies.

#### 5.4.2. Formation Mechanism for High-Velocity Anomalies

The SENAM has experienced multiple magmatic events that can lead to the emplacement of plutons within the crust (Withjack et al., 2013). Among these events, the magmatism associated with the CAMP has been interpreted to have the largest intensity and form abundant basaltic dikes along the coastal plain (Marzoli et al., 1999, 2018). Furthermore, the horizontal distribution of high-velocity anomalies in our model roughly correlates with the CAMP-related basaltic dikes in Virginia, northeastern and central North Carolina, and northern South Carolina (Figure 9a). We hypothesize that the intra-crustal high-velocity anomalies observed within the SENAM continent likely represent the solidified magma reservoirs formed during the CAMP emplacement. In this case, the basaltic magma associated with the CAMP migrates from the upper mantle into the crust, assimilates the surrounding rocks and develops reservoirs. The crystal fractionation of magma within these reservoirs produced dense, mafic igneous rocks at depth and erupted less dense, basaltic rocks at the surface (Cruden & Weinberg, 2018; Petford et al., 2000). In addition, the magmatic injection probably leads to the depression of the Moho beneath the High Vs 2 and High Vs 3 (Figure 5f; Cross-sections AA' and BB' in Figure 6).

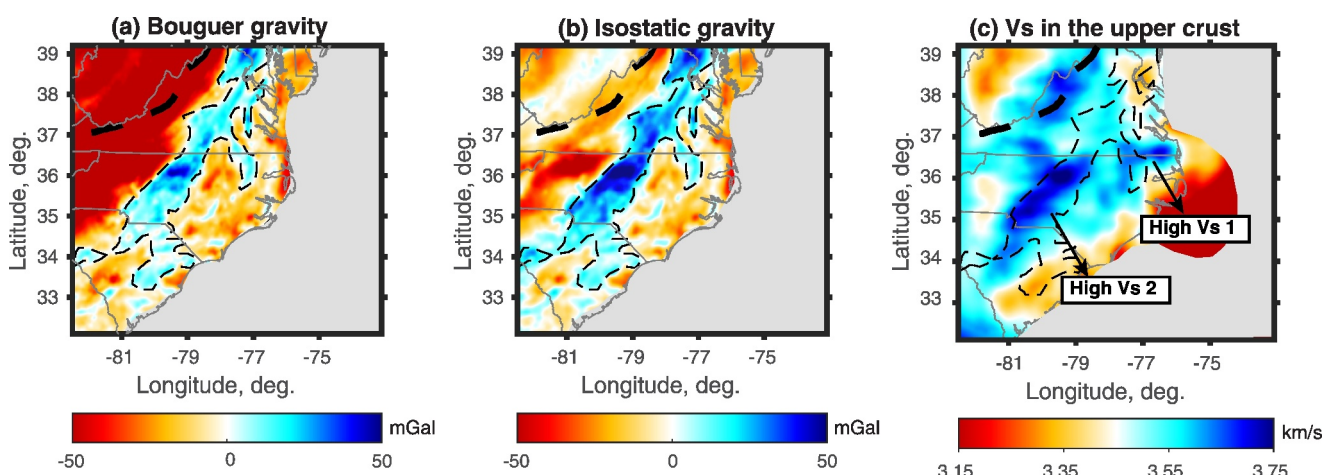


**Figure 8.** Comparison between gravity anomalies and the average velocity of the upper crust from our model. (a and b) are Bouguer gravity anomaly and isostatic gravity anomaly, respectively. (c) Shear-wave velocities within the upper crust averaged between 4 and 10 km depths. The black dashed lines mark the positive anomalies observed in two types of gravity data.

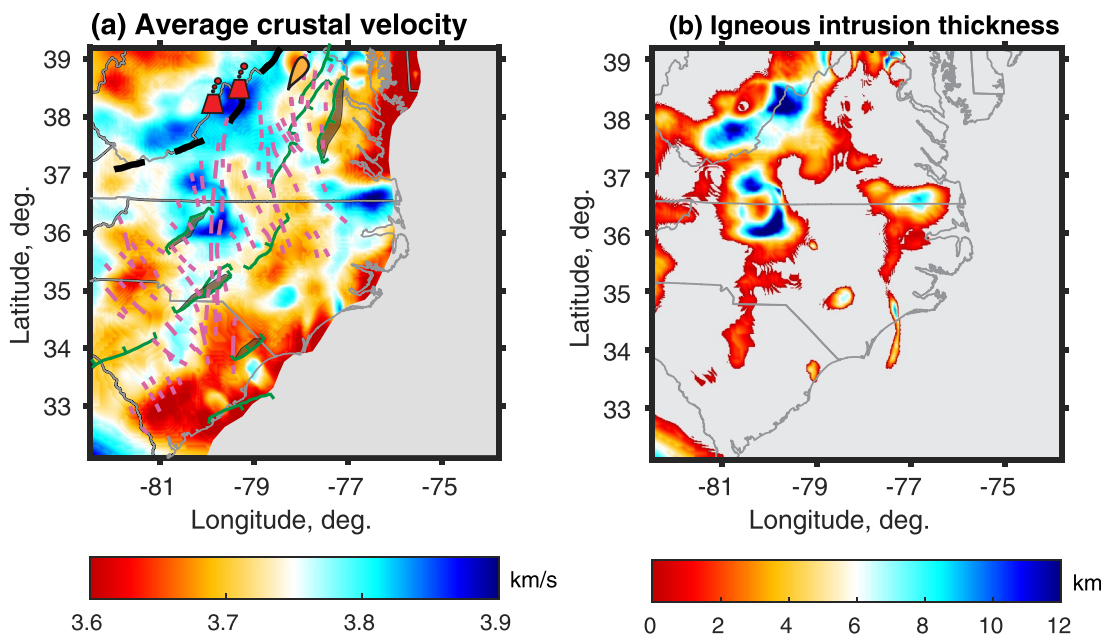


**Figure 9.** (a) Average velocity of the crustal layer between the 4 km depth and the depth for the 4.2 km/s contour. Brown patches represent the rift basins in our study region. Other symbols are same to those in Figure 1a. (b) The thickness of intrusive igneous rocks estimated based on the average crustal velocity using a linear equation by Withjack et al. (2013).

#### 5.4.3. Tectonic Implications From High-Velocity Anomalies

The observations of the high-velocity anomalies in our model provide several new and important tectonic implications about the CAMP magmatism. First, our model reveals a vertical distribution of the CAMP magmatic intrusion from ~6 km depth downward to the lower crust. In contrast, previous studies in southern New England and southern Georgia suggest that the CAMP intrusion is confined to the lower crust (e.g., Gao et al., 2020; Marzen et al., 2020). The divergent observations between ours and previous studies may indicate varying intensities of the CAMP intrusion along the entire passive margin. The modeling study by Beutel (2009) suggests that the CAMP magmatism varies in intensity, which results in a highly non-uniform distribution of basaltic dikes on the surface of the passive margin. It is likely that the CAMP magmatism in our study region exhibits a greater intensity, leading to a larger volume of magmatic intrusion compared to other portions of the margin.

Second, the 3-D distribution of high-velocity anomalies in our model allows us to estimate the volumes of intruded magma in the continental crust of the SENAM (Please see the details of magma volume estimation in Supporting Information S1). Based on our estimation, the intrusive igneous rocks in the SENAM have a general thickness of 2–6 km, with several local-scale maximum values of 8–12 km along the Appalachian Front and in central and northeastern North Carolina (Figure 9). The total estimated volumes of intruded magmas in the SENAM are ~586,000 km<sup>3</sup>. Assuming that all of these magmatic intrusions in our study region are associated with CAMP, they constitute ~19% of its entire estimated volume (~3-million-km<sup>3</sup>; Marzoli et al., 2018). Further studies are needed to refine the estimation of the CAMP magma volume.

Third, our model has an implication for the formation mechanism of the CAMP. Previous seismic imaging studies suggest that the CAMP magmatic intrusion primarily concentrates beneath the rift basins along the passive margin, and they thus attributed its formation to the lithospheric thinning during Mesozoic rifting (e.g., Gao et al., 2020; Marzen et al., 2020). However, the distribution of the high-velocity anomalies observed in our model extends beyond the rift basins in the SENAM, implying an alternative formation mechanism (Figure 9a). One possibility is that the CAMP magmatism is triggered by a convection cell of the upper mantle with melts due to the lithospheric thickness variation between the craton and the passive margin. Several modeling studies have demonstrated this possibility (e.g., King & Anderson, 1995; McHone, 2000; McHone et al., 2005). Moreover, the High Vs 3 in our model roughly distributes along the tectonic boundary between the craton and the SENAM (Figures 7e, 7f, and 9a), further supporting this hypothesis.

## 6. Conclusions

We constructed a high-resolution 3-D crustal model in the SENAM with a combination of multimodal dispersion inversion and full-waveform ambient noise tomography. Our new model recognizes a transitional zone between the oceanic and continental portion over a horizontal distance of ~100–150 km, which features a large difference in both sedimentary thickness and Moho depth. In addition, our model reveals three high-velocity anomalies within the continental crust of the SENAM, with a velocity of 3.75–4.0 km/s and a mushroom-/dome-shaped geometry. We propose that magmatic intrusions associated with the CAMP facilitated the thinning of the continental crust across the coastline, forming a narrow oceanic-continent transitional crust. The CAMP emplacement probably caused widespread magmatic intrusion within the continental crust of the SENAM, which were subsequently solidified into high-velocity plutons. These findings shed new lights on the magmatic modification of crustal structures beneath passive margins.

## Data Availability Statement

All the seismic data used in this study are available on the website of the IRIS Data Management Center. The seismic networks include the South Carolina Seismic Network (University of South Carolina, 1987), the CERI Southern Appalachian Seismic Network, the US Geological Survey Network (Albuquerque Seismological Laboratory/USGS, 1980), the Lamont-Doherty Cooperative Seismographic Network (Lamont Doherty Earth Observatory, Columbia University, 1970), the Central and Eastern US Network (Albuquerque Seismological Laboratory/USGS, 2013), the Cooperative New Madrid Seismic Network the NetQuakes Network (U.S. Geological Survey, 1989), the Southeastern Appalachian Cooperative Seismic Network, the South Carolina Earth Physics Project (University of South Carolina, 2000), the Single Station Network (IRIS, 1970), the EarthScope US Transportable Array (IRIS Transportable Array, 2003), the US National Seismic Network (Albuquerque Seismological Laboratory/USGS, 1990), the Central Virginia and South Carolina Seismic Monitoring Experiment (Chapman, 2017), the Mid-Atlantic Geophysical Integrative Collaboration Network (Long & Wiita, 2013), the Pre-Hydrofracking Regional Assessment of Central Carolina Seismicity Network (Wagner, 2012), the RAMP Virginia Network (Meltzer, 2011), the Eastern North American Community Seismic Experiment (Gaherty, 2014), and the Appalachian Seismic Transect (Wagner, 2009). The velocity model generated by this study is available in Li (2024) and through requests to the authors upon publication of this work. The computer codes in this study are available in Li (2024) and Li et al. (2021) or through requests to the authors above.

## Acknowledgments

This research was supported by the National Natural Science Foundation of China (Grants 42104052, 41974043, and 42174058), the fellowship of the China Postdoctoral Science Foundation (Grant 2022M711473) and the Guangdong Provincial Key Laboratory of Geophysical High-resolution Imaging Technology (2022B1212010002). The computational resources used in this study were supported by the Center for Computational Science and Engineering at Southern University of Science and Technology. We thank Dr. Zhengbo Li and Dr. Wei Zhang for their constructive suggestions.

## References

- Albuquerque Seismological Laboratory (ASL)/USGS. (1980). U.S. Geological survey networks [Dataset]. *International Federation of Digital Seismograph Networks*. <https://doi.org/10.7914/SN/GS>
- Albuquerque Seismological Laboratory (ASL)/USGS. (1990). United States national seismic network [Dataset]. *International Federation of Digital Seismograph Networks*. <https://doi.org/10.7914/SN/US>
- Albuquerque Seismological Laboratory/USGS. (2013). Central and eastern US network [Dataset]. *International Federation of Digital Seismograph Networks*. <https://doi.org/10.7914/SN/N4>
- Austin, J. A., Stoffa, P. L., Phillips, J. D., Oh, J. Y., Sawyer, D. S., Purdy, G. M., et al. (1990). Crustal structure of the southeast Georgia embayment Carolina trough: Preliminary results of a composite seismic image of a continental suture and a volcanic passive margin. *Geology*, 18(10), 1023–1027. [https://doi.org/10.1130/0091-7613\(1990\)018<1023:csotsg>2.3.co;2](https://doi.org/10.1130/0091-7613(1990)018<1023:csotsg>2.3.co;2)
- Bailey, D. G., & Lupulescu, M. V. (2015). Spatial, temporal, mineralogical, and compositional variations in Mesozoic kimberlitic magmatism in New York State. *Lithos*, 212, 298–310. <https://doi.org/10.1016/j.lithos.2014.11.022>
- Bankey, V., Cuevas, A., Daniels, D., Finn, C. A., Hernandez, I., & Hill, P. (2002). Digital data grids for the magnetic anomaly map of North America, Open-File Report 02–414. *United States Geologic Survey*.
- Bécel, A., Davis, J. K., Shuck, B. D., Van Avendonk, H. J. A., & Gibson, J. C. (2020). Evidence for a prolonged continental breakup resulting from slow extension rates at the eastern North American volcanic rifted margin. *Journal of Geophysical Research: Solid Earth*, 125(9), e2020JB020093. <https://doi.org/10.1029/2020JB020093>
- Behn, M. D., & Lin, J. (2000). Segmentation in gravity and magnetic anomalies along the U.S. East Coast passive margin: Implications for incipient structure of the oceanic lithosphere. *Journal of Geophysical Research*, 105(B11), 25769–25790. <https://doi.org/10.1029/2000JB900292>
- Beutel, E. K. (2009). Magmatic rifting of Pangaea linked to onset of South American plate motion. *Tectonophysics*, 468(1–4), 149–157. <https://doi.org/10.1016/j.tecto.2008.06.019>
- Bialas, R. W., Buck, W. R., & Qin, R. (2010). How much magma is required to rift a continent? *Earth and Planetary Science Letters*, 292(1–2), 68–78. <https://doi.org/10.1016/j.epsl.2010.01.021>
- Bodin, T., & Sambridge, M. (2009). Seismic tomography with the reversible jump algorithm. *Geophysical Journal International*, 178(3), 1411–1436. <https://doi.org/10.1111/j.1365-246X.2009.04226.x>
- Bodin, T., Sambridge, M., Tkalcic, H., Arroucau, P., Gallagher, K., & Rawlinson, N. (2012). Transdimensional inversion of receiver functions and surface wave dispersion. *Journal of Geophysical Research*, 117(B2), B02301. <https://doi.org/10.1029/2011JB008560>

- Bonvalot, S., Balmino, G., Briais, A., Kuhn, M., Peyrefitte, A., Vales, N., et al. (2012). *World gravity map (scale 1:50000000)*. BGI-CGMW-CNRS-IRD.
- Bowden, D. C., Kohler, M. D., Tsai, V. C., & Weeraratne, D. S. (2016). Offshore southern California lithospheric velocity structure from noise cross-correlation functions. *Journal of Geophysical Research: Solid Earth*, 121(5), 3415–3427. <https://doi.org/10.1002/2016JB012919>
- Buck, W. R. (2004). Consequences of asthenospheric variability on continental rifting. In *Rheology and deformation of the lithosphere at continental margins* (Vol. 62, pp. 1–30). Columbia University Press. <https://doi.org/10.7312/karn12738-002>
- Buck, W. R. (2006). The role of magma in the development of the Afro-Arabian rift system. *Geological Society of London, Special Publication*, 259(1), 43–54. <https://doi.org/10.1144/gsl.sp.2006.259.01.05>
- Cao, W., Kaus, B. J. P., & Paterson, S. (2016). Intrusion of granitic magma into the continental crust facilitated by magma pulsing and dyke–diapir interactions: Numerical simulations. *Tectonics*, 35(6), 1575–1594. <https://doi.org/10.1002/2015TC004076>
- Chapman, M. (2017). Central Virginia and South Carolina seismic monitoring experiment [Dataset]. *International Federation of Digital Seismograph Networks*. [https://doi.org/10.7914/SN/5H\\_2017](https://doi.org/10.7914/SN/5H_2017)
- Christensen, N. I., & Stanley, D. (2003). Seismic velocities and densities of rocks. *International Geophysics*, 81, 1587–1594. [https://doi.org/10.1016/S0074-6142\(03\)80278-4](https://doi.org/10.1016/S0074-6142(03)80278-4)
- Coltice, N., Phillips, B. R., Bertrand, H., Ricard, Y., & Rey, P. (2007). Global warming of the mantle at the origin of flood basalts over supercontinents. *Geology*, 35(5), 391–394. <https://doi.org/10.1130/G23240A.1>
- Connolly, J. A. D. (2009). The geodynamic equation of state: What and how. *Geochemistry, Geophysics, Geosystems*, 10(10), Q10014. <https://doi.org/10.1029/2009GC002540>
- Cruden, A. R., & Weinberg, R. F. (2018). Mechanisms of magma transport and storage in the lower and middle crust–magma segregation, ascent and emplacement. In *Volcanic and igneous plumbing systems: Understanding magma transport, storage, and evolution in the Earth's crust* (pp. 13–53). Elsevier. <https://doi.org/10.1016/B978-0-12-809749-6.00002-9>
- Dalton, C. A., & Faul, U. H. (2010). The oceanic and cratonic upper mantle: Clues from joint interpretation of global velocity and attenuation models. *Lithos*, 120(1), 160–172. <https://doi.org/10.1016/j.lithos.2010.08.020>
- Daniels, K. A., Bastow, I. D., Keir, D., Sparks, R. S. J., & Menand, T. (2014). Thermal models of dyke intrusion during development of continent-ocean transition. *Earth and Planetary Science Letters*, 385, 145–153. <https://doi.org/10.1016/j.epsl.2013.09.018>
- Davis, J. K., Bécel, A., & Buck, W. R. (2018). Estimating emplacement rates for seaward-dipping reflectors associated with the US East Coast magnetic anomaly. *Geophysical Journal International*, 215(3), 1594–1603. <https://doi.org/10.1093/gji/ggy360>
- Dick, H. J. B., Lin, J., & Schouten, H. (2003). An ultraslow-spreading class of ocean ridge. *Nature*, 426(6965), 405–412. <https://doi.org/10.1038/nature02128>
- Dreiling, J., & Tilmann, F. (2019). BayHunter–McMC transdimensional Bayesian inversion of receiver functions and surface wave dispersion. *GFZ Data Services*. <https://doi.org/10.5880/GFZ.2.4.2019.001>
- Dunbar, J. A., & Sawyer, D. S. (1989). How preexisting weaknesses control the style of continental breakup. *Journal of Geophysical Research*, 94(B6), 7278–7292. <https://doi.org/10.1029/jb094b06p07278>
- Franke, D. (2013). Rifting, lithosphere breakup and volcanism: Comparison of magma-poor and volcanic rifted margins. *Marine and Petroleum Geology*, 43, 63–87. <https://doi.org/10.1016/j.marpetgeo.2012.11.003>
- Gaherty, J. (2014). Eastern North American margin community seismic experiment [Dataset]. *International Federation of Digital Seismograph Networks*. [https://doi.org/10.7914/SN/YO\\_2014](https://doi.org/10.7914/SN/YO_2014)
- Gao, H., & Shen, Y. (2014). Upper mantle structure of the Cascades from full-wave ambient noise tomography: Evidence for 3D mantle upwelling in the back-arc. *Earth and Planetary Science Letters*, 309, 222–233. <https://doi.org/10.1016/j.epsl.2014.01.012>
- Gao, H., Yang, X., Long, M. D., & Aragon, J. C. (2020). Seismic evidence for crustal modification beneath the Hartford rift basin in the northeastern United States. *Geophysical Research Letters*, 47(17), e2020GL089316. <https://doi.org/10.1029/2020GL089316>
- U.S. Geological Survey. (1989). NetQuakes [Dataset]. *International Federation of Digital Seismograph Networks*. <https://doi.org/10.7914/SN/NQ>
- Guo, W., Zhao, S., Wang, F., Yang, Z., Jia, S., & Liu, Z. (2019). Crustal structure of the eastern Piedmont and Atlantic coastal plain in North Carolina and Virginia, eastern North American margin. *Earth Planets and Space*, 71(1), 69. <https://doi.org/10.1186/s40623-019-1049-z>
- Hatcher, R. D. (2010). The Appalachian orogen: A brief summary, from Rodinia to Pangea: The lithotectonic record of the Appalachian region. *Geological Society of America Memoir*, 206, 1–19. [https://doi.org/10.1130/2010.1206\(01\)](https://doi.org/10.1130/2010.1206(01))
- Holbrook, W. S., Reiter, E. C., Purdy, G. M., Sawyer, D., Stoffa, P. L., Austin, J. A., et al. (1994). Deep structure of the United States Atlantic continental margin, offshore South Carolina, from coincident ocean bottom and multichannel seismic data. *Journal of Geophysical Research*, 99(B5), 9155–9178. <https://doi.org/10.1029/93jb01821>
- Hole, M. J. (2015). The generation of continental flood basalts by decompression melting of internally heated mantle. *Geology*, 43(4), 311–314. <https://doi.org/10.1130/G36442.1>
- Hu, S., Luo, S., & Yao, H. (2020). The frequency-Bessel spectrograms of multicomponent cross-correlation functions from seismic ambient noise. *Journal of Geophysical Research: Solid Earth*, 125(8). <https://doi.org/10.1029/2020JB019630>
- Incorporated Research Institutions For Seismology. (1970). Single station [Dataset]. *International Federation of Digital Seismograph Networks*. <https://doi.org/10.7914/SN/SS>
- IRIS Transportable Array. (2003). USAArray transportable array [Dataset]. *International Federation of Digital Seismograph Networks*. <https://doi.org/10.7914/SN/TA>
- Kelemen, P. B., & Holbrook, W. S. (1995). Origin of thick, high-velocity igneous crust along the US East Coast margin. *Journal of Geophysical Research*, 100(B6), 10077–10094. <https://doi.org/10.1029/95jb00924>
- King, S. D., & Anderson, D. L. (1995). An alternative mechanism of flood basalt formation. *Earth and Planetary Science Letters*, 136(3–4), 269–279. [https://doi.org/10.1016/0012-821X\(95\)00205-Q](https://doi.org/10.1016/0012-821X(95)00205-Q)
- Kinney, S. T., MacLennan, S. A., Keller, C. B., Schoene, B., Setera, J. B., VanTongeren, J. A., & Olsen, P. E. (2021). Zircon U-Pb geochronology constrains continental expression of Great Meteor Hotspot magmatism. *Geophysical Research Letters*, 48(11), e2020GL091390. <https://doi.org/10.1029/2020GL091390>
- Lamont Doherty Earth Observatory (LDEO), Columbia University. (1970). Lamont-Doherty cooperative seismographic network [Dataset]. *International Federation of Digital Seismograph Networks*. <https://doi.org/10.7914/SN/LD>
- Lang, G., ten Brink, U. S., Hutchinson, D. R., Mountain, G. S., & Schattner, U. (2020). The role of premagmatic rifting in shaping a volcanic continental margin: An example from the Eastern North American Margin. *Journal of Geophysical Research: Solid Earth*, 125(11), e2020JB019576. <https://doi.org/10.1029/2020JB019576>

- Leleu, S., & Hartley, A. J. (2010). Controls on the stratigraphic development of the Triassic Fundy Basin, Nova Scotia: Implications for the tectonostratigraphic evolution of Triassic Atlantic rift basins. *Journal of the Geological Society*, 167(3), 437–454. <https://doi.org/10.1144/0016-76492009-092>
- Li, C. (2024). The open science framework repository. [Dataset and Software]. <https://osf.io/wq6bu/>
- Li, C., & Gao, H. (2021). Modification of crust and mantle lithosphere beneath the southern part of the eastern North American passive margin. *Geophysical Research Letters*, 48(16), e2020GL090555. <https://doi.org/10.1029/2020GL090555>
- Li, C., Gao, H., & Williams, M. L. (2020). Seismic characteristics of the eastern North American crust with Ps converted waves: Terrane accretion and modification of continental crust. *Journal of Geophysical Research: Solid Earth*, 125(5), e2019JB018727. <https://doi.org/10.1029/2019JB018727>
- Li, Z., Zhou, J., Wu, G., Wang, J., Zhang, G., Dong, S., et al. (2021). CC-FJPy: A Python package for seismic ambient noise cross-correlation and the frequency-Bessel transform method. *Seismological Research Letters*, 92(5), 3179–3186. <https://doi.org/10.1785/0220210042>
- Lizarralde, D., & Holbrook, W. S. (1997). U.S. mid-Atlantic margin structure and early thermal evolution. *Journal of Geophysical Research*, 102(B10), 22855–22875. <https://doi.org/10.1029/96JB03805>
- Long, M., & Wiita, P. (2013). Mid-Atlantic geophysical integrative collaboration [Dataset]. *International Federation of Digital Seismograph Networks*. [https://doi.org/10.7914/SN/7A\\_2013](https://doi.org/10.7914/SN/7A_2013)
- Lynner, C., & Porritt, R. W. (2017). Crustal structure across the eastern North American margin from ambient noise tomography. *Geophysical Research Letters*, 44(13), 6651–6657. <https://doi.org/10.1002/2017GL073500>
- Ma, X., & Lowry, A. R. (2017). USArray imaging of continental crust in the conterminous United States. *Tectonics*, 36(12), 2882–2902. <https://doi.org/10.1002/2017TC004540>
- Marzen, R. E., Shillington, D. J., Lizarralde, D., Knapp, J. H., Heffner, D. M., Davis, J. K., & Harder, S. H. (2020). Limited and localized magmatism in the Central Atlantic Magmatic Province. *Nature Communications*, 11(1), 3397. <https://doi.org/10.1038/s41467-020-17193-6>
- Marzoli, A., Callegaro, S., Dal Corso, J., Davies, J. H., Chiaradà, M., Youbi, N., et al. (2018). The central Atlantic magmatic province (CAMP): A review. In *The late Triassic world* (pp. 91–125). Springer.
- Marzoli, A., Renne, P. R., Piccirillo, E. M., Ernesto, M., Bellieni, G., & De Min, A. (1999). Extensive 200-million-year-old continental flood basalts of the Central Atlantic Magmatic Province. *Science*, 284(5414), 616–618. <https://doi.org/10.1126/science.284.5414.616>
- Mazza, S. E., Gazel, E., Johnson, E. A., Kunk, M. J., McAleer, R., Spotila, J. A., et al. (2014). Volcanoes of the passive margin: The youngest magmatic event in eastern North America. *Geology*, 42(6), 483–486. <https://doi.org/10.1130/G35407.1>
- Mazza, S. E., Gazel, E. A., Johnson, E. A., Bizimis, M., McAleer, R., & Biriyol, C. B. (2017). Post-rift magmatic evolution of the eastern North American “passive-aggressive” margin. *Geochemistry, Geophysics, Geosystems*, 18(1), 3–22. <https://doi.org/10.1002/2016GC006646>
- McHone, J. G. (2000). Non-plume magmatism and rifting during the opening of the central Atlantic Ocean. *Tectonophysics*, 316(3–4), 287–296. [https://doi.org/10.1016/S0040-1951\(99\)00260-7](https://doi.org/10.1016/S0040-1951(99)00260-7)
- McHone, J. G., Anderson, D. L., Beutel, E. K., & Fialko, Y. A. (2005). Giant dikes, rifts, flood basalts, and plate tectonics: A contention of mantle models. In G. R. Foulger, J. H. Natland, D. C. Presnall, & D. L. Anderson (Eds.), *Plates, plumes, and paradigms*. Geological society of America special paper (Vol. 388, pp. 401–420). [https://doi.org/10.1130/2005.2388\(24\)](https://doi.org/10.1130/2005.2388(24))
- Meltzer, A. (2011). RAMP Virginia [Dataset]. *International Federation of Digital Seismograph Networks*. [https://doi.org/10.7914/SN/YC\\_2011](https://doi.org/10.7914/SN/YC_2011)
- Pagli, C., Mazzarini, F., Keir, D., Rivalta, E., & Rooney, T. O. (2015). Introduction: Anatomy of rifting: Tectonics and magmatism in continental rifts, oceanic spreading centers, and transforms. *Geosphere*, 11(5), 1256–1261. <https://doi.org/10.1130/GES01082.1>
- Petford, N., Cruden, A. R., McCaffrey, K. J. W., & Vigneresse, J. L. (2000). Granite magma formation, transport and emplacement in the Earth’s crust. *Nature*, 408(6813), 669–673. <https://doi.org/10.1038/35047000>
- Ragland, P. C., Cummins, L. E., & Arthur, J. D. (1992). Compositional patterns for early Mesozoic diabases from South Carolina to central Virginia. In J. H. Puffer, & P. C. Ragland (Eds.), *Eastern North American Mesozoic magmatism*. Geological Society of America Special Paper 268.
- Russell, J. B., & Gaherty, J. B. (2021). Lithosphere structure and seismic anisotropy offshore eastern North America: Implications for continental breakup and ultra-slow spreading dynamics. *Journal of Geophysical Research: Solid Earth*, 126(12), e2021JB022955. <https://doi.org/10.1029/2021JB022955>
- Savage, B., Covellone, B. M., & Shen, Y. (2017). Wave speed structure of the eastern North American margin. *Earth and Planetary Science Letters*, 459, 394–405. <https://doi.org/10.1016/j.epsl.2016.11.028>
- Shen, W., & Ritzwoller, M. H. (2016). Crustal and uppermost mantle structure beneath the United States. *Journal of Geophysical Research: Solid Earth*, 121(6), 4306–4342. <https://doi.org/10.1002/2016JB012887>
- Sheridan, R. E., Musser, D. L., Glover, L., Talwani, M., Ewing, J. I., Holbrook, W. S., et al. (1993). Deep seismic reflection data of edge United States mid-Atlantic continental margin experiment implications for Appalachian sutures and Mesozoic rifting and magmatic Underplating. *Geology*, 21(6), 563–567. [https://doi.org/10.1130/0091-7613\(1993\)021<0563:Dsrdoe>2.3.Co;2](https://doi.org/10.1130/0091-7613(1993)021<0563:Dsrdoe>2.3.Co;2)
- Shuck, B. D., Van Avendonk, H. J., & Bécel, A. (2019). The role of mantle melts in the transition from rifting to seafloor spreading offshore eastern North America. *Earth and Planetary Science Letters*, 525, 115756. <https://doi.org/10.1016/j.epsl.2019.115756>
- Talwani, M., Ewing, J., Sheridan, R. E., Holbrook, W. S., & Glover, L. (1995). The edge experiment and the US East Coast magnetic anomaly. E. Banda, M. Torne, & M. Talwani (Eds.), In *Rifted ocean-continent boundaries* (Vol. 463, pp. 155–181). Kluwer Academic. [https://doi.org/10.1007/978-94-011-0043-4\\_9](https://doi.org/10.1007/978-94-011-0043-4_9)
- Tian, X., & Buck, W. R. (2019). Lithospheric thickness of volcanic rifting margins: Constraints from seaward dipping reflectors. *Journal of Geophysical Research: Solid Earth*, 124(4), 3254–3270. <https://doi.org/10.1029/2018JB016733>
- Torsvik, T. H., Burke, K., Steinberger, B., Webb, S. J., & Ashwal, L. D. (2010). Diamonds sampled by plumes from the core-mantle boundary. *Nature*, 466(7304), 352–355. <https://doi.org/10.1038/nature09216>
- University of South Carolina. (1987). South Carolina seismic network [Dataset]. *International Federation of Digital Seismograph Networks*. <https://doi.org/10.7914/SN/CO>
- University of South Carolina. (2000). South Carolina Earth physics project [Dataset]. *International Federation of Digital Seismograph Networks*. <https://doi.org/10.7914/SN/SP>
- Wagner, L. (2009). Appalachian seismic transect [Dataset]. *International Federation of Digital Seismograph Networks*. [https://doi.org/10.7914/SN/Z4\\_2009](https://doi.org/10.7914/SN/Z4_2009)
- Wagner, L. (2012). Pre-hydrofracking regional assessment of Central Carolina seismicity [Dataset]. *International Federation of Digital Seismograph Networks*. [https://doi.org/10.7914/SN/XQ\\_2012](https://doi.org/10.7914/SN/XQ_2012)
- Wagner, L. S., Fischer, K. M., Hawman, R., Hopper, E., & Howell, D. (2018). The relative roles of inheritance and long-term passive margin lithospheric evolution on the modern structure and tectonic activity in the southeastern United States. *Geosphere*, 14(4), 1385–1410. <https://doi.org/10.1130/GES01593.1>

- Wang, J., Wu, G., & Chen, X. (2019). Frequency-Bessel transform method for effective imaging of higher-mode Rayleigh dispersion curves from ambient seismic noise data. *Journal of Geophysical Research: Solid Earth*, 124(4), 3708–3723. <https://doi.org/10.1029/2018JB016595>
- Withjack, M. O., Schlische, R. W., Malinconico, M. L., & Olsen, P. E. (2013). Rift-basin development: Lessons from the Triassic-Jurassic Newark basin of eastern North America. In *Geological society, London, special publications*, W. U. Mohriak, A. Danforth, P. J. Post, D. E. Brown, G. C. Tari, M. Nemčok, et al. (Eds.). *Conjugate divergent margins*, (Vol. 369, pp. 301–321). Geological Society, London, Special Publications. <https://doi.org/10.1144/sp369.13>
- Wright, T. J., Sigmundsson, F., Pagli, C., Belachew, M., Hamling, I. J., Brandsdóttir, B., et al. (2012). Geophysical constraints on the dynamics of spreading centres from rifting episodes on land. *Nature Geoscience*, 5(4), 242–250. <https://doi.org/10.1038/ngeo1428>
- Wu, G. X., Pan, L., Wang, J. N., & Chen, X. (2020). Shear velocity inversion using multimodal dispersion curves from ambient seismic noise data of USArray transportable array. *Journal of Geophysical Research: Solid Earth*, 125(1), e2019JB018213. <https://doi.org/10.1029/2019JB018213>
- Wyer, P., & Watts, A. (2006). Gravity anomalies and segmentation at the East Coast, USA continental margin. *Geophysical Journal International*, 166(3), 1015–1038. <https://doi.org/10.1111/j.1365-246x.2006.03066.x>
- Xu, W., Lithgow-Bertelloni, C., Stixrude, L., & Ritsema, J. (2008). The effect of bulk composition and temperature on mantle seismic structure. *Earth and Planetary Science Letters*, 25(1–2), 70–79. <https://doi.org/10.1016/j.epsl.2008.08.012>
- Yang, Y., & Ritzwoller, M. H. (2008). Characteristics of ambient seismic noise as a source for surface wave tomography. *Geochemistry, Geophysics, Geosystems*, 9(2), Q02008. <https://doi.org/10.1029/2007GC001814>
- Zhang, H. L., Ravat, D., & Lowry, A. R. (2020). Crustal composition and Moho variations of the central and eastern United States: Improving resolution and geologic interpretation of EarthScope USArray seismic images using gravity. *Journal of Geophysical Research: Solid Earth*, 125(3), e2019JB018537. <https://doi.org/10.1029/2019JB018537>

## References From the Supporting Information

- Bell, S. W., Forsyth, D. W., & Ruan, Y. (2015). Removing noise from the vertical component records of ocean-bottom seismometers: Results from year one of the Cascadia initiative. *Bulletin of the Seismological Society of America*, 105(1), 300–313. <https://doi.org/10.1785/0120140054>
- Crawford, W. C., & Webb, S. C. (2000). Identifying and removing tilt noise from low frequency (<0.1 Hz) seafloor vertical seismic data. *Bulletin of the Seismological Society of America*, 90(4), 952–963. <https://doi.org/10.1785/0119990121>
- Janiszewski, H. A., Gaherty, J. B., Abers, G. A., Gao, H., & Eilon, Z. C. (2019). Amphibious surface-wave phase-velocity measurements of the Cascadia subduction zone. *Geophysical Journal International*, 217(3), 1929–1948. <https://doi.org/10.1093/gji/ggz051>
- Lévêque, J. J., Rivera, L., & Wittlinger, G. (1993). On the use of the checker-board test to assess the resolution of tomographic inversions. *Geophysical Journal International*, 115(1), 313–318. <https://doi.org/10.1111/j.1365-246X.1993.tb05605.x>
- Nishida, K. (2017). Ambient seismic wave field. *Proceedings of the Japan Academy Series B Physical and Biological Sciences*, 93(7), 423–448. <https://doi.org/10.2183/pjab.93.026>
- Peterson, J. (1993). *Observations and modeling of seismic background noise*. (Technical Report). U. S. Geological Survey Open File Report.
- Rawlinson, N., & Spakman, W. (2016). On the use of sensitivity tests in seismic tomography. *Geophysical Journal International*, 205(2), 1221–1243. <https://doi.org/10.1093/gji/ggw084>
- Spakman, W., & Nolet, G. (1988). Imaging algorithms, accuracy, and resolution in delay time tomography. In N. J. Vlaar, G. Nolet, M. J. R. Wortel, & S. A. P. Cloetingh (Eds.), *Mathematical geophysics: A survey of recent developments in seismology and geodynamics* (pp. 155–187). Springer.